Anthropogenic activity at the Leyte geothermal field promoted the 2017 Mw 6.5 earthquake

Wenbin Xu[1], Hua Gao[2], Roland Burgmann[3], Guangcai Feng[4], Zhiwei Li[1], and Guoyan Jiang[2]

[1]Central South University
[2]Wuhan University
[3]University of California, Berkeley
[4]Laboratory of Radar Remote Sensing, School of Geosciences and Info-Physics, Central South University

November 23, 2022

Abstract

Recent studies of anthropogenically induced seismicity have improved our understanding of the causal relationships between earthquakes and industrial activity. Whether larger-magnitude earthquakes can be triggered and how human injection and production of fluids interact with active faults remain poorly understood. The 2017 Mw 6.5 Leyte earthquake nucleated at a depth near the production zone and within 1 km of an actively producing geothermal field in the Philippines. We use satellite radar data to constrain the pre-earthquake ground deformation across the field and the Leyte fault and to determine the coseismic source parameters. From consideration of regional historical seismicity and fluid extraction model constrained by fluid injection and extraction rates, we find evidence suggesting that the mainshock is directly associated with the geothermal production efforts. Our findings demonstrate that the extraction of geothermal power close to active fault zones is capable of triggering damaging earthquakes, a hazard that was previously underappreciated.

Anthropogenic activity at the Leyte geothermal field promoted the 2017 M_w 6.5 earthquake

Wenbin Xu[1,*], Hua Gao[2], Roland Bürgmann[3], Guangcai Feng[1], Zhiwei Li[1], Guoyan Jiang[4]

[1]School of Geosciences and Info-Physics, Central South University, Changsha 410083, China
[2]State Key Laboratory of Information Engineering in Surveying, Mapping, and Remote Sensing, Wuhan University, Wuhan 430079, China.
[3]Department of Earth and Planetary Science, University of California, Berkeley, California, USA
[4]School of Geodesy and Geomatics, Wuhan University, Wuhan, China
*Correspondence to: wenbin.xu@csu.edu.cn

Key Points:

- The 2017 Leyte earthquake occurred close to the active Leyte geothermal field
- Ground deformation and fault slip of the mainshock and the largest aftershock are studied
- Geothermal energy extraction close to active fault systems can trigger major earthquakes

Abstract: Recent studies of anthropogenically induced seismicity have improved our understanding of the causal relationships between earthquakes and industrial activity. Whether larger-magnitude earthquakes can be triggered and how human injection and production of fluids interact with active faults remain poorly understood. The 2017 Mw 6.5 Leyte earthquake nucleated at a depth close to the production zone and within 1 km of an actively producing geothermal field in the Philippines. Here we use satellite radar data to constrain the pre-earthquake ground deformation across the field and the Leyte fault and to determine the coseismic source parameters. From consideration of regional historical seismicity and fluid extraction model constrained by fluid injection and extraction rates, we find evidence suggesting that the mainshock is directly associated with the geothermal production efforts. Our findings demonstrate that the extraction of geothermal power close to active fault zones is capable of triggering damaging earthquakes, a hazard that was previously underappreciated.

Plain Language Summary

The 2017 Leyte earthquake took place close to the Leyte Geothermal Production Field in the Philippines, which is one the largest active geothermal areas in the world. We carefully study the preseismic and coseismic deformation to determine the fault source parameters and slip distributions. We find a concentrated peak slip patch at depths between 2 and 5 km just below the injection and extraction depth. Combining regional historical seismicity and fluid extraction model, we further examine whether the 2017 mainshock was directly triggered by geothermal energy extraction in the Leyte geothermal field, thus representing a rupture that was initiated by anthropogenic forcing but grew beyond the bounds of the region directly affected by fluid-pressure. The results of this study help shed light on the triggering mechanism of the mainshock.

1. Introduction

The injection of fluids into deep wells and poroelastic stress changes from fluid withdrawal alter the stresses and strains in the earth's crust and can cause earthquakes (Brodsky & Lajoie, 2013, Ellsworth, 2013, Shirzaei et al., 2016, Keranen & Weingarten, 2018). The strongest injection-related M_w 5.8 Pawnee, Oklahoma earthquake reported to date was related to wastewater disposal (Manga et al., 2016). The largest well-documented event caused by enhanced geothermal systems activity to date was the 2017 M_w 5.5 Pohang earthquake in South Korea (Grigoli et al., 2018, Kim et al., 2018). In the Philippines, the Leyte geothermal production field is one of the world's largest liquid-dominated reservoirs, located close to the central Philippine fault (Fig. 1a). The designed capacity of this geothermal field is 700.9 MW of energy. Massive extraction and fluid injection efforts have accelerated in the Leyte geothermal production field with commissions of two additional power plants since the last commission in 1997 (Prioul et al., 2000, Uribe et al., 2015). The monthly fluid injection rate increased by nearly five times from 1996 to 1998 and leveled off at ~1.3 million tons per year after 2000 (Apuada et al., 2005, Uribe et al., 2015). In total, about 350 million tons of fluids were injected into the reservoir at ~2 km depth between 1996 and 2012, while approximately 760 million tons were extracted. As has been observed in other geothermal fields (e.g., Deichmann & Giardini, 2009; Trugman et al., 2016), the number of seismic events in the Leyte geothermal production field has increased significantly in response to the accelerated fluid injection and extraction (Fig. 1b).

On July 6, 2017, a M_w 6.5 seismic event occurred on the Leyte segment of the central Philippine fault within the Leyte geothermal production field (Fig. 1). Three people were killed, and 448 were injured (NDRRMC, 2017). The epicenter of the mainshock was located ~15 km northeast of Ormoc, the island's largest city that has a population of more than 0.2 million (Census of Population, 2015). As reported by the Philippine Institute of Volcanology and Seismology (PHIVOLCS), the mainshock was widely felt around the region and caused numerous landslides and soil liquefaction near its epicenter (PHIVOLCS, 2017a). The mainshock was followed by ~800 $M \geq 1.5$ aftershocks in the first week (PHIVOLCS, 2017a). The largest aftershock (M_w 5.8) occurred about 13 km southeast of the mainshock on July 10 (PHIVOLCS, 2019). The mainshock rupture extended along the north central Leyte fault segment from Lake Danao in the south to Lemon in the north with a length of ~26 km (PHIVOLCS, 2017b). The largest aftershock ruptured from near Lake Danao towards the south for a further ~12 km along another fault segment. The seismic moment tensor solutions for the July 6 and 10 events show that the seismogenic fault is oriented in a north-northwest direction with eastward dip angles between 70° and 85° (USGS, 2019). The Philippine seismic network shows that the hypocenters of the July 6 and 10 events were located at 2 km and 3 km depth, respectively (PHIVOLCS, 2019). The existing geodetic studies of this earthquake showed that the majority of coseismic fault slip is concentrated at the shallow depth near the Leyte geothermal field (Yang et al., 2018; Fukushima et al., 2019; Dianala et al., 2020). The epicenter of the mainshock is located at 1 km from the Mahanagdong geothermal field and is within 10 km from the other major wells and power plants of the Leyte geothermal field. The latter is located closest to the epicenter. The close proximity of geothermal wells and power plants to the shallow mainshock hypocenter and the apparent correlation between increased production activity and seismicity raise the question if the recent 2017 event was triggered by human activity or represent natural tectonic events.

2. Data and Inversion Method

2.1. Coseismic InSAR data processing

The lack of local micro-seismicity and recent injection and production data does not allow to track the diffusion of the pore-pressure in the subsurface. Therefore, we need to rely on satellite remote sensing and global network data to assess the potential interaction of injected fluids with the seismogenic fault. We used three pairs of SAR data from both the ascending (Feb. 13, 2016 - Jul. 15, 2017) and descending (Jun. 3 - Jul. 15, 2017) orbits of ALOS-2 and the descending Sentinel-1 orbit (Jul. 1 - Jul. 13, 2017) to obtain interferograms covering the July 6 and 10 events (Fig. 1). The wavelength of the L-band ALOS-2 radar (23.6 cm) is more than four times longer than the C-band Sentinel-1 data (5.6 cm). The ALOS-2 data maintain better interferometric quality in regions near the seismogenic fault. The GAMMA software was used to generate and unwrap interferograms (Wegmuller & Werner, 1997). The 1-arcsecond Shuttle Radar Topography Mission Digital Elevation Model was used to simulate and remove the terrain phase from the interferograms. The Goldstein adaptive filtering method was used to reduce the noise in interferograms. To improve the data quality, we masked out the low coherence data and manually adjusted unwrapping errors by shifting the phase by integer multiples of 2π (Fig. 2). We also used the offset tracking technique (Michel et al., 1999) to calculate range offset maps from both the ascending and descending ALOS-2 data (Fig. S1). The azimuth offsets of the ALOS-2 data and offset measurements of Sentinel-1 data are noisy and not used in the study. The quadtree sampling algorithm was used to downsample InSAR data and offset measurements (Jónsson et al., 2002). A total of 888 InSAR points and 252 offset points were obtained after quadtree downsampling.

2.2 Pre-earthquake InSAR Time Series Processing

We used the small baseline subset interferometric synthetic aperture radar method (Berardino et al., 2002) to process the ascending (Feb 10, 2007 to Feb 21, 2011) and descending (Oct 12, 2006 to Jan 23, 2011) ALOS PALSAR and Sentinel-1 images (Table S1). Firstly, we generated the differential interferometric pairs from ALOS PALSAR with multilook 6:16 (range: azimuth) and Sentinel-1 20: 4 (range: azimuth). Then, we selected high quality points by jointly considering amplitude dispersion, intensity and mean coherence of pixels in differential interferograms. In the SBAS-InSAR procedure, multiple linear regression was performed to determine the linear deformation, topographic error and residual phase. The standard deviation of linear regression process was used to filter poor quality points. Based on the height corrections, deformation velocity and atmospheric delay from the linear regression process, we obtained the refined unwrapped phase. We generated the raw time series displacements using the singular value decomposition method. The residual phase was extracted after removing the linear deformation component. The residual phase mainly consists of nonlinear deformation, atmospheric delay and phase noise. The phase noise is random in the temporal and spatial domains. Therefore, the temporal high-pass filtering, and spatial low-pass filtering were performed to remove atmospheric delay. Finally, the time series displacements and deformation rate were obtained.

2.3 Inversion for fault source parameters

As our InSAR data span both the July 6 and 10 events, we chose to construct a two-fault model to simultaneously estimate the fault geometry and the spatially variable slip distribution of both events. Because the north central Leyte fault has been well mapped by PHIVOLCS (2017a), we fixed the surface trace of the Leyte fault segment as the top edge of the modeled fault. Therefore, the dip angles and slip values are the only unknown parameters that need to be determined. We first used the downsampled surface deformation data and the particle swarm optimization (PSO) algorithm (Eberhart & Kennedy, 1995) to carry out the nonlinear search for the best-fit dip angles. To determine the relative weight between different datasets, we normalized InSAR data from different orbits and platforms by using their own norms and equally weighted these data in the model optimization. The mean values obtained from 100 parameter searches were taken as the optimal source parameters, as shown in Table S2. The Monte-Carlo analysis (Metropolis & Ulam, 1949) was carried out to assess the uncertainties.

After determining the fault geometry, we extended the width of the large (the modeled fault hosting the M_w 6.5 July 6 event) and small (the modeled fault of the M_w 5.8 July 10 event) faults to ~19 km and ~10 km, respectively. To better resolve shallow fault slip, we designed a data-driven fault patch discretization method (Tong et al., 2010). The size of patches ranges from 0.46 to 1.33 km^2 for the large fault and 0.42 to 2.02 km^2 for the small fault (Fig. 3). Finally, we used a non-negative least-squares algorithm to constrain thrust-slip and left-lateral strike-slip components to ensure that the calculations are stable. The function model of the inversion is

$$\begin{cases} \begin{bmatrix} \boldsymbol{d} \\ \mathbf{0} \\ \mathbf{0} \end{bmatrix} = \begin{bmatrix} \mathbf{G}_{\mathrm{ss}} & \mathbf{G}_{\mathrm{ds}} \\ \lambda \mathbf{H}_{\mathrm{ss}} & \mathbf{0} \\ \mathbf{0} & \lambda \mathbf{H}_{\mathrm{ds}} \end{bmatrix} \begin{bmatrix} \boldsymbol{m}_{\mathrm{ss}} \\ \boldsymbol{m}_{\mathrm{ds}} \end{bmatrix} + \begin{bmatrix} \boldsymbol{\varepsilon} \\ \mathbf{0} \\ \mathbf{0} \end{bmatrix}, \\ \boldsymbol{m}_{\mathrm{ss}} \geq \mathbf{0}, \boldsymbol{m}_{\mathrm{ds}} \geq \mathbf{0} \end{cases} \tag{1}$$

where $\boldsymbol{d}$ indicates the downsampled InSAR and offset data. $\mathbf{G}_{\text{ss}}$ and $\mathbf{G}_{\text{ds}}$ are the Green's function matrix of the strike-slip $\boldsymbol{m}_{\text{ss}}$ and the dip-slip $\boldsymbol{m}_{\text{ds}}$ component, respectively. $\mathbf{H}_{\text{ss}}$ and $\mathbf{H}_{\text{ds}}$ are the Laplace smoothing constraint matrices of $\boldsymbol{m}_{\text{ss}}$ and $\boldsymbol{m}_{\text{ds}}$, respectively, $\boldsymbol{\varepsilon}$ is the error, and λ is the smoothing factor used to balance the observations and the smoothness matrix. We selected the smoothing factor based on visual examination of the trade-off curve of the roughness and the root-mean-square (RMS) value (Xu et al., 2017).

2.4 Calculation of fluid extraction model

We used 900 laterally distributed Mogi-sources with a spacing of 0.5 km to model the observed complex surface deformation pattern at the Leyte geothermal field following a similar first-order approach taken in a previous study (Trugmann et al., 2014). All the sources are placed at a depth of 2 km, which is consistent with the production depth. Assuming a homogeneous, isotropic and elastic medium, the displacement vector (u_x, u_y, u_z) at the surface $(x, y, z = 0)$ can be modeled by a single Mogi source at position $(x_0, y_0, z_0 < 0)$ as follows:

$$\begin{bmatrix} u_x \\ u_y \\ u_z \end{bmatrix} = \frac{(1-v)\Delta V}{\pi} \begin{bmatrix} (x - x_0)/R^3 \\ (y - y_0)/R^3 \\ (z - z_0)/R^3 \end{bmatrix}$$

Where $R = \sqrt{(x - x_0)^2 + (y - y_0)^2 + (z - z_0)^2}$ represents the distance between the source and data and ΔV is the volume change (Mogi, 1958). The observed deformation is the sum of the distributed Mogi. Because the depth of the Mogi sources is fixed, the volume changes can be inverted using a regularized least-squares inversion. Once the fluid extraction model is determined, we can calculate the Coulomb stress changes using the following three steps: firstly, we generalized the Fourier domain approach of Steketee (1958) to obtain the Green's function for a radial point source. Then, we convoluted the Green's function and source distribution to obtain the full 3D stress tensor field surrounding the field. Finally, the local shear, fault-normal and Coulomb stress components can be resolved using the estimated 2017 Leyte fault plane parameterization.

3. Results

The ALOS-2 interferograms maintain good coherence near the epicenter, except in the mountainous regions to the east of the ruptured fault (Fig. 2, a and b). The ascending ALOS-2 interferogram shows ~24 cm of coseismic deformation in the radar line-of-sight direction (LOS) on the west side of the fault. The descending ALOS-2 interferogram shows up to 40 cm of deformation in the LOS direction, although atmospheric artifacts in this interferogram appear to be strong. The far-field ground deformation of the descending Sentinel-1 data is well preserved, but coherence is lost near the fault trace (Fig. 2c). SAR pixel offset measurements are not affected by interferometric coherence and can be used to obtain the near-fault coseismic deformation (Xu et al., 2017). The range pixel offsets, obtained from both the descending and ascending ALOS-2 data (Fig. S1), show more than 1 m of coseismic offset across the fault close to the epicenter, where the InSAR phases are decorrelated. The sense of surface displacements suggests that the event is dominated by slip on the left-lateral fault strike slip and is consistent with the focal mechanism.

The finite fault slip distribution model of the July 6 event shows a concentrated peak slip patch of up to 3.8 m at depths between 2 and 5 km (Fig. 3a). The maximum fault slip zone is bounded by the Tongonan-1 power plant in the Leyte geothermal field and the hypocenter. From the highest slip patch to the periphery, the coseismic slip decreases relatively smoothly towards the north and the surface. The estimated moment release for the July 6 event is 4.69×10^{18} Nm (M_w 6.4), assuming a shear modulus of 30 GPa. Most of the fault slip on the southern fault segment, likely associated with the largest aftershock, occurred at depths shallower than 10 km. The estimated moment release on the southern fault segment is 1.63×10^{18} Nm, equivalent to M_w 6.1, suggesting that some of the slip on this segment may have occurred during the mainshock, rather than just the M_w 5.8 aftershock. The fault slip of both events is characterized by a dominant component of left-lateral strike slip with a minor east-side-up reverse motion near the surface (Fig. S2). Obvious spatial variability in the slip is seen on the main fault near the surface. The modeled shallow slip is in good agreement with the field-measured surface displacements along the rupture trace (Table S3), especially near the epicenter (Fig. 3a and Fig. S2a). The model predictions agree well with the coseismic LOS surface displacements (Fig. 2d and e), with RMS misfit of 2.4 cm and 3.9 cm for the ascending and descending ALOS-2 interferograms, respectively. The unexplained signals seen in the residuals are located mostly near the surface rupture, which might be due to the presence of inelastic deformation or the simplified geometry of our model rupture (Vallage et al., 2015). The Sentinel-1 data do not preserve good coherence in the near field, but the model predictions fit the far field data well with an RMS value of 1.6 cm (Fig. 2f). The best-fitting model also captures the main signals of the range offsets with RMS misfits of 66.2 cm for the ascending data and 24.9 cm for the descending data, respectively (Fig. S1). These residuals are within the expected range considering that the precision of offset measurements is about one tenth of a pixel dimension (Michel et al., 1999). Our fault slip model also matches well with the existing studies (Yang et al., 2018; Fukushima et al., 2019; Dianala et al., 2020). Checkerboard resolution tests show that the shallow fault slip of both July 6 and 10 events is well recovered by our data (Fig. S3).

4. Discussion and Conclusions

It can be difficult to distinguish between natural and anthropogenic earthquakes (e.g., Keranen and Weingarten, 2018). Both pore-pressure diffusion and poroelastic stresses have been considered as potential sources of triggering (e.g., Goebel and Brodsky, 2018). The role of increased pore pressure due to fluid injection in decreasing the effective normal stress on preexisting, highly-stressed faults, and thus promoting failure, is well documented (Suckale, 2009).

The following lines of evidence support that the mainshock was directly related to human activity in the region. The hypocenter of the 2017 event and injection wells are located very close to each other. The closest distance between the bottom of wells in the Mahanagdong field and the hypocenter is about 1 km (Fig. 4a). The temporal coincidence between injection and production activities and the onset of microseismicity is high (Fig. 1b). Very little seismicity was recorded by either global or local seismological networks until the accelerated injection and production activities in 1997. Although the recorded waveforms of the 1947 Ms 6.9 event show a high similarity with the 2017 mainshock (Fukushima et al., 2019), the epicenter of the 1947 event is located ~25 km north of the 2017 mainshock, suggesting it did not nucleate near the Leyte geothermal field. More recently, Dianala et al., (2020) used an interseismic fault coupling model to argue that the 2017 and 1947 events may have ruptured the same locked section of the Leyte fault. This is similar to the 2017 M_w 5.4 Pohang earthquake sequence, which is found to be triggered by fluid from an enhanced geothermal system site (Kim et al., 2018). The Pohang event was preceded by a deep tectonic earthquake, potentially on the same fault system. Thus, there is an obvious link between the two largest potentially triggered seismic events in geothermal reservoirs and previously seismically active faults that bound or traverse the reservoir. The occurrence of the 2017 events after about two decades of injection and extraction activity suggests that the human-induced stress changes advanced failure on the locked portions of the northern part of the central Leyte fault and triggered the 2017 earthquake, which was likely in an advanced phase of its tectonic loading cycle (Dianala et al., 2020).

The spatial extent and magnitude of surface displacement at the Leyte geothermal field preceding the 2017 event show a maximum subsidence rate of ~3 cm/yr close to the Tongonan powerplant (Fig. 4, Fig. S4 and Table S1). The ascending data show the subsidence center at the geothermal wells and extending to the fault., while the descending data show a further surface movement towards the satellite along the fault. This difference is mainly due to the different viewing geometry in the ascending and descending orbits. These observations agree with the findings of previous studies (Fukushima et al., 2019; Dianala et al., 2020). The ground deformation is primarily associated with fluid over-extraction at the Leyte geothermal field. Fluid extraction changes the shear and normal stresses acting on nearby faults and can thus induce faulting events surrounding a reservoir depending on their location and orientation in the evolving stress field (Segall, 1989). We model the surface displacement rates from different satellite orbits using a distribution of finely spaced volumetric Mogi sources and then compute the Coulomb stress changes on the 2017 Leyte rupture zone (Trugman et al., 2014). Our laterally heterogeneous volume-loss model shows that the net anthropogenic fluid extraction rate between 2006 and 2017 at the Leyte geothermal field is about 1.7×10^6 m^3/yr. Although the estimated volume decrease is too small to account for the recorded over-extraction volume, the discrepancy might be explained by 1). this estimated volume change represents that of the reservoir chamber but not the subsurface fluid volume change; 2). this estimated volume does not consider fluid compressibility (Rivalta and Segall, 2008). Our simple fluid extraction model represents a first-order approximation, the calculated Coulomb stress changes of up to 0.3 MPa/yr on the 2017 Leyte rupture zone indicate the net fluid extraction due to human activities likely played a role in the timing of the 2017 event

(Fig. 4b). One of limitations of the modeling is ignoring the poroelastic stress changes associated with fluid extraction and injection that were found to trigger earthquakes (Segall, 1989; González et al., 2012; Goebel and Brodsky, 2018).

All of the presented evidence falls well within the classical criteria for assessing triggered seismicity (Davis & Frohlich, 1993; Dahm et al., 2015; Frohlich et al., 2016; Verdon et al., 2019) and support the causal relationship between the recent over-extraction associated with geothermal energy production and the 2017 seismic failure. Surface deformation data inversion confirms that substantial overproduction and associated Coulomb stress perturbation are the possible drivers for the recent seismic activity. Attention needs to be paid to the exploration of geothermal resources close to active fault systems, both in this region and worldwide.

Acknowledgments

We thank the reviewers for their helpful comments. We thank D. Trugman for helpful discussion on elastic volume strain modeling. This work was funded by the National Key R&D Program of China (2019YFC1509205) and by the National Natural Science Foundation of China (No. 41804015). The ALOS-1 and ALOS-2 data were provided by JAXA (http://en.alospasco.com) under a contract of the 6th Research Announcement for ALOS-2 (Nos. 3124 and 1390) and the Sentinel-1A data by ESA/Copernicus (https://scihub.copernicus.eu). Several figures were prepared by using the Generic Mapping Tools software. The processed data used in the study are available at https://github.com/Wenbin16/Leytedata.

References

Apuada, N. A., Olivar, R. E. R., & Salonga, N. D. (2005). Repeat microgravity and leveling surveys at Leyte geothermal production field, North Central Leyte, Philippines. Extraction, 4, 5. Available at: https://www.geothermal-energy.org/pdf/IGAstandard/WGC/2005/0711.pdf, last accessed June 2019.

Brodsky, E. E., & Lajoie, L. J. (2013). Anthropogenic seismicity rates and operational parameters at the Salton Sea Geothermal Field. *Science*, 341(6145), 543-546. https://doi.org/10.1126/science.1239213.

Caranto, J.A., & Jara, M.P. (2015). Factors controlling reservoir permeability at the Leyte Geothermal Field, Philippines. Proceedings World Geothermal Congress 2015 Melbourne, Australia, 19-25 April 2015.

Census of Population. (2015). "Region VIII (Eastern Visayas)". Total Population by Province, City, Municipality and Barangay. PSA. Available at: https://www.psa.gov.ph/sites/default/files/attachments/hsd/pressrelease/R08.xlsx, last accessed June 2019.

Dahm, T., S. Cesca, S. Hainzl, T. Braun, and F. Krüger (2015), Discrimination between induced, triggered, and natural earthquakes close to hydrocarbon reservoirs: A probabilistic approach based on the modeling of depletion-induced stress changes and seismological source parameters, *J. Geophys. Res. Solid Earth*, 120, 2491–2509, doi:10.1002/2014JB011778.

Davis, S. D., & C. Frohlich (1993), Did (or will) fluid injection cause earthquakes? Criteria for a rational assessment, *Seismol. Res. Lett.*, 64, 207– 224.

Deichmann, N., & D. Giardini (2009), Earthquakes induced by the stimulation of an enhanced geothermal system below Basel (Switzerland), *Seismol. Res. Lett.*, 80, 784–798.

Dianala, J. D. B., Jolivet, R.,Thomas, M. Y., Fukushima, Y.,Parsons, B., & Walker, R. (2020). Therelationship between seismic andaseismic slip on the Philippine Faulton Leyte Island: Bayesian modeling offault slip and geothermal subsidence. *J. Geophys. Res. Solid Earth*, 125, e2020JB020052. https://doi.org/10.1029/2020JB020052.

Duquesnoy, T., Barrier, E., Kasser, M., Aurelio, M., Gaulon, R., Punongbayan, R. S., & Rangin, C. (1994). Detection of creep along the Philippine fault: First results of geodetic measurements on Leyte island, central Philippine. *Geophys. Res. Lett.*, 21(11), 975-978. https://doi.org/10.1029/94GL00640.

Eberhart, R. & Kennedy, J. (1995). A new optimizer using particle swarm theory. Micro Machine and Human Science. MHS'95., Proceedings of the Sixth International Symposium on. IEEE, 1995: 39-43. https://doi.org/10.1109/MHS.1995.494215.

Ellsworth, W. L. (2013). Injection-induced earthquakes, *Science*, 341, 142.

Ellsworth, W. L., Giardini, D., Townend, J., Ge, S., & Shimamoto, T. (2019). Triggering of the Pohang, Korea, earthquake (M w 5.5) by enhanced geothermal system stimulation. Seismological Research Letters, 90(5), 1844-1858. https://doi.org/10.1785/0220190102.

Frohlich, C., DeShon, H., Stump, B., Hayward, C., Hornbach, M., & Walter, J. I. (2016). A historical review of induced earthquakes in Texas. *Seismol. Res. Lett.*, 87(4), 1022– 1038. https://doi.org/10.1785/0220160016

Fukushima, Y., Hashimoto, M., Miyazawa, M. et al. (2019). Surface creep rate distribution along the Philippine fault, Leyte Island, and possible repeating of Mw ~ 6.5 earthquakes on an isolated locked patch. *Earth Planets Space*, 71, 118. https://doi.org/10.1186/s40623-019-1096-5.

Goebel, T. H., & Brodsky, E. E. (2018). The spatial footprint of injection wells in a global compilation of induced earthquake sequences. *Science*, 361(6405), 899– 904. https://doi.org/10.1126/science.aat5449.

González, P. J., Tiampo, K. F., Palano, M., Cannavó, F., & Fernández, J. (2012). The 2011 Lorca earthquake slip distribution controlled by groundwater crustal unloading. *Nature Geoscience*, 5(11), 821–825. https://doi.org/10.1038/ngeo1610

Grigoli, F., Cesca, S., Rinaldi, A. P., Manconi, A., López-Comino, J. A., Clinton, J. F., ... & Wiemer, S. (2018). The November 2017 Mw 5.5 Pohang earthquake: A possible case of induced seismicity in South Korea. *Science*, 360(6392), 1003-1006. https://doi.org/10.1126/science.aat2010.

Jónsson, S., Zebker, H., Segall, P., & Amelung, F. (2002). Fault slip distribution of the 1999 M w 7.1 Hector Mine, California, earthquake, estimated from satellite radar and GPS measurements. Bulletin of the Seismological Society of America, 92(4), 1377-1389. https://doi.org/10.1785/0120000922.

Keranen, K. M., & Weingarten, M. (2018). Induced seismicity. *Annu. Rev. Earth Planet. Sci.*, 46, 149– 174. https://doi.org/10.1146/annurev-earth-082517-010054.

Kim, K. H., Ree, J. H., Kim, Y., Kim, S., Kang, S. Y., & Seo, W. (2018). Assessing whether the 2017 Mw 5.4 Pohang earthquake in South Korea was an induced event. *Science*, 360(6392), 1007–1009. https://doi.org/10.1126/science.aat6081

King, G. C. P., Stein, R. S., & Lin, J. (1994). Static stress changes and the triggering of earthquakes. *Bull. Seismol. Soc. Am.*, 84(3), 935–953.

Kiyoo, M. O. G. I. (1958). Relations between the eruptions of various volcanoes and the deformations of the ground surfaces around them. Earthq Res Inst, 36, 99-134.

Lee, K.-K., W. L. Ellsworth, D. Giardini, J. Townend, S. Ge, T. Shimamoto, I.-W. Yeo, T.-S. Kang, J. Rhie, D.-H. Sheen, et al. (2019). Managing injection-induced seismic risks, *Science,* 364, 730–732, doi: 10.1126/science.aax1878.

Manga, M., Wang, C. Y., & Shirzaei, M. (2016). Increased stream discharge after the 3 September 2016 Mw 5.8 Pawnee, Oklahoma earthquake. *Geophys. Res. Lett.*, 43(22), 11588-11594. https://doi.org/10.1002/2016GL071268.

Metropolis, N., Ulam, S. (1949). The monte carlo method. Journal of the American statistical association, 44(247), 335-341. https://doi.org/10.1080/01621459.1949.10483310.

Michel, R., Avouac, J. P., & Taboury, J. (1999). Measuring ground displacements from SAR amplitude images: Application to the Landers earthquake. *Geophys. Res. Lett.*, 26(7), 875-878.

NDRRMC (2017). Sitrep No.23 re Magnitude 6.5 Earthquake in Ormoc City, Leyte. Available at: https://reliefweb.int/report/philippines/ndrrmc-update-sitrep-no-23-re-magnitude-65-earthquake-ormoc-city-leyte-06-august , last accessed June 2019.

PHIVOLCS (2017a). The 06 July 2017 Magnitude 6.5 Leyte Earthquake. Available at: https://www.phivolcs.dost.gov.ph/index.php/news/638-poster-of-the-06-july-2017-magnitude-6-5-earthquake-in-leyte-2, last accessed June 2019.

PHIVOLCS (2017b). Ground rupture of the Philippine fault: Leyte segment. Available at: https://satreps.phivolcs.dost.gov.ph/index.php?option=com_content&view=article&id=7652:surface-rupture-of-the-2017-m65-leyte-earthquake-along-the-philippine-fault-surigao-segment&catid=60:latest-news&Itemid=19, last accessed June 2019.

PHIVOLCS. (2019). PHIVOLCS Earthquake Bulletins: latest earthquake information. Available at: https://www.phivolcs.dost.gov.ph/index.php/earthquake/earthquake-information3, last accessed June 2019.

Prioul et al. (2000), An induced seismicity experiment across a creeping segment of the Philippine Fault, *J. Geophys. Res.*, 105(B6):13,595-13,612, doi: 10.1029/2000JB900052.

Rivalta, E., & Segall, P. (2008). Magma compressibility and the missing source for some dike intrusions. Geophysical Research Letters, 35(4). https://doi.org/10.1029/2007GL032521.

Segall, P. (1989). Earthquakes triggered by fluid extraction, *Geology,* 17, 942-946.

Shirzaei, M., Ellsworth, W. L., Tiampo, K. F., González, P. J., & Manga, M. (2016). Surface uplift and time-dependent seismic hazard due to fluid injection in eastern Texas. *Science*, 353(6306), 1416-1419. doi: 10.1126/science.aag0262.

Steketee, J. A. (1958). On Volterra's dislocations in a semi-infinite elastic medium. Canadian Journal of Physics, 36(2), 192-205. https://doi.org/10.1139/p58-024.

Suckale, J., (2009). Induced seismicity in hydrocarbon fields. *Adv. Geophys.*, 51, 55–106.

Tong, X., Sandwell, D. T., & Fialko, Y. (2010). Coseismic slip model of the 2008 Wenchuan earthquake derived from joint inversion of interferometric synthetic aperture radar, GPS, and field data. Journal of Geophysical Research: Solid Earth, 115(B4). https://doi.org/10.1029/2009JB006625.

Trugman, D. T., A. A. Borsa, & D. T. Sandwell (2014), Did stresses from the Cerro Prieto Geothermal Field influence the El Mayor-Cucapah rupture sequence?, *Geophys. Res. Lett.*, 41, doi:10.1002/ 2014GL061959.

Trugman, D. T., P. M. Shearer, A. A. Borsa, & Y. Fialko (2016), A comparison of long-term changes in seismicity at The Geysers, Salton Sea, and Coso geothermal fields, *J. Geophys. Res. Solid Earth*, 121, doi:10.1002/2015JB012510.

United States Geological Survey (USGS). (2019). Available at: https://earthquake.usgs.gov/earthquakes/search/, last accessed June 2019.

Uribe, M. H. C, Dacillo, D. B., Dacoag, L. M., Andrino, R. P., & Alcober, E. H. (2015). 30 Years of Tongonan-1 (Leyte, Philippines) Sustained Production. Proceedings World Geothermal Congress 2015 Melbourne, Australia, 19-25 April 2015.

Vallage, A., Klinger, Y., Grandin, R., Bhat, H. S., & Pierrot-Deseilligny, M. (2015). Inelastic surface deformation during the 2013 Mw 7.7 Balochistan, Pakistan, earthquake. *Geology*, 43(12), 1079-1082. https://doi.org/10.1130/G37290.1.

Verdon, J. P., Baptie, B. J., & Bommer, J. J. (2019). An improved framework for discriminating seismicity induced by industrial activities from natural earthquakes. *Seismol. Res. Lett.*, 90(4), 1592– 1611. https://doi.org/10.1785/0220190030.

Wegmuller, U. & Werner, C. (1997). Retrieval of vegetation parameters with SAR interferometry. IEEE Transactions on Geoscience and Remote Sensing, 35(1): 18-24. https://doi.org/10.1109/36.551930.

Wetzler, N., Shalev, E., Göbel, T., Amelung, F., Kurzon, I., Lyakhovsky, V., & Brodsky, E. E. (2019). Earthquake Swarms Triggered by Groundwater Extraction Near the Dead Sea Fault. *Geophys. Res. Lett.*, 46(14), 8056–8063. https://doi.org/10.1029/2019GL083491.

Xu, W., Rivalta, E., & Li, X. (2017). Magmatic architecture within a rift segment: Articulate axial magma storage at Erta Ale volcano, Ethiopia. *Earth Planet. Sci. Lett.*, 476, 79-86. https://doi.org/10.1016/j.epsl.2017.07.051.

Yang, Y. H., Tsai, M. C., Hu, J. C., Aurelio, M. A., Hashimoto, M., Escudero, J. A. P., Escudero, Z. Su, & Chen, Q. (2018). Coseismic slip deficit of the 2017 Mw 6.5 Ormoc earthquake that occurred along a creeping segment and geothermal field of the Philippine Fault. *Geophys. Res. Lett.*, 45(6), 2659-2668. https://doi.org/10.1002/2017GL076417.

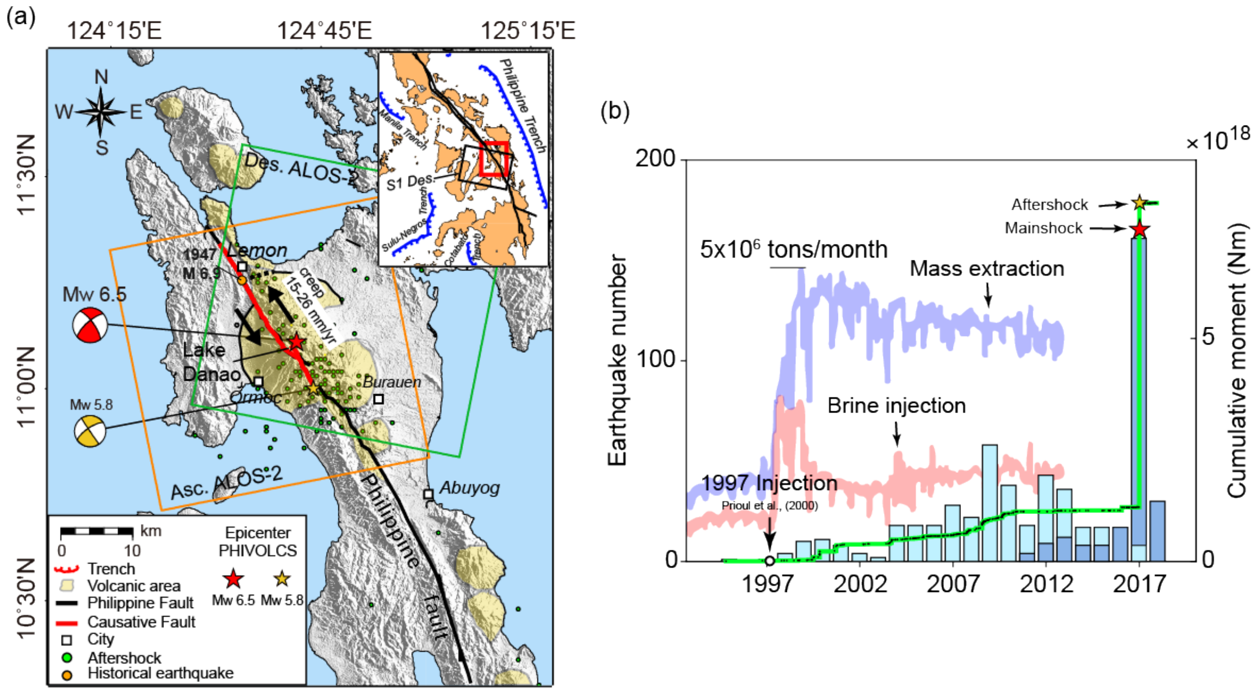

Fig. 1. The 2017 events and the correlation between seismicity and injection. (a) Regional tectonic map. The color-coded focal mechanisms represent the epicenters of the mainshock (red) and its largest aftershock (yellow) from PHIVOLCS. Green dots show M > 2.0 aftershocks within the first 25 days (sourced from PHIVOLCS, 2019). Orange dot represent the location of the 1947 earthquake. Black line represents the Philippine fault. Bold red line represents the location of the modeled fault. Color-coded rectangles represent the coverage of ALOS-2 data. Yellow areas represent the volcanic fields adopted from Duquesnoy et al. (1994). The inset shows the study area (red rectangle). The black rectangle in the inset represents the coverage of Sentinel-1 data. (b) the correlation between cumulative seismic moment release (green line), number of events per year (ISC: light blue bar, PHIVOLCS: dark blue bar), the 1997 injection experiment (white dot) and the two events (color coded stars) at the Leyte geothermal production field. The volume of monthly mass extraction and brine injection (Uribe et al., 2015) are shown in light purple and pink, respectively.

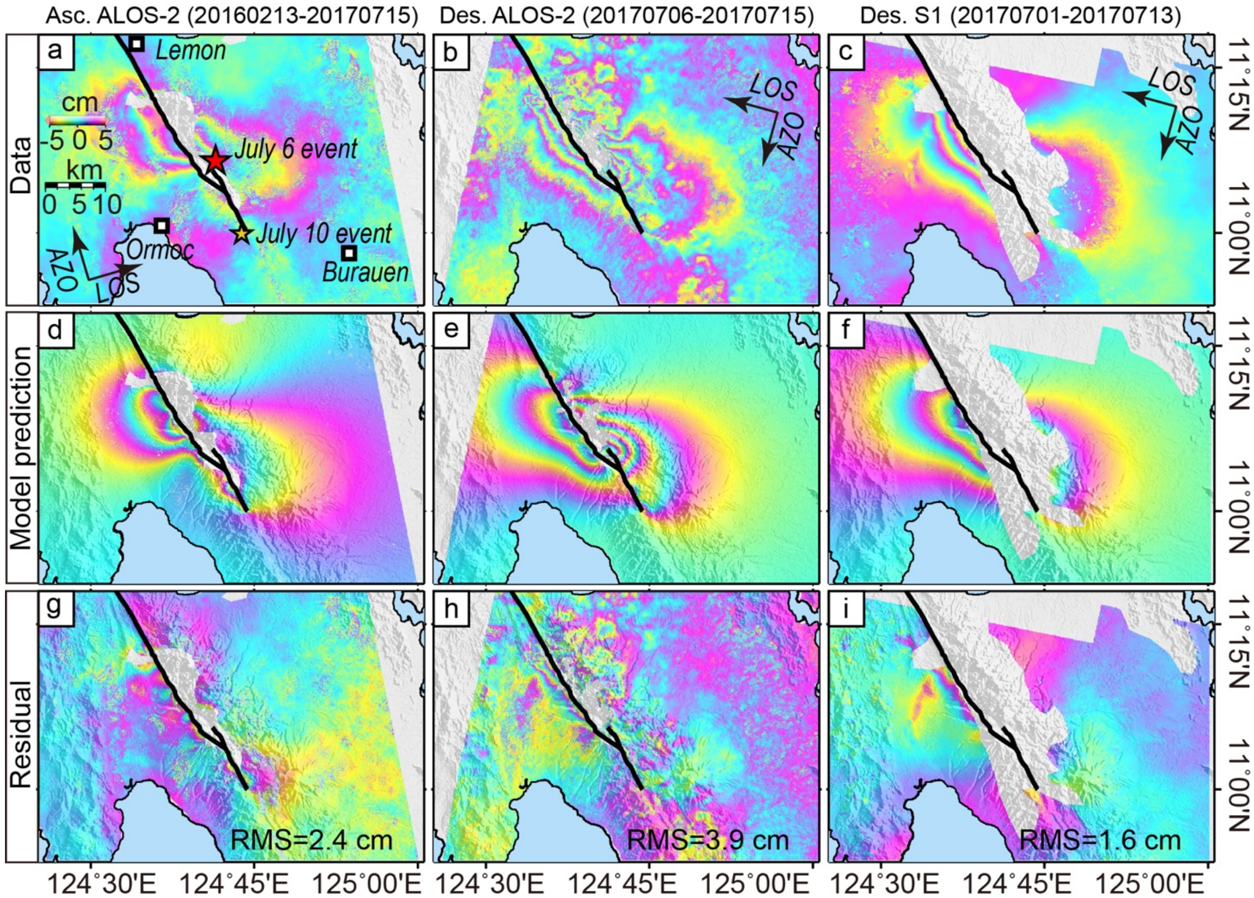

Fig. 2. Crustal deformation and model prediction of the mainshock and its largest aftershock. Unwrapped and then rewrapped (a) ascending and (b) descending ALOS-2 data and (c) Sentinel-1 used in this study. Each fringe corresponds to a rewrapped line-of-sight displacement of 10 cm. Color coded triangles represent the locations of major regional geothermal power plants. Yellow diamonds represent the major injection and production wells (Apuada et al., 2005). (d-f) Predicted InSAR data from the optimal model. (g-i) residuals. Stars represent the epicenter of the mainshock (red) and the largest aftershock (orange) event, respectively. The bold black line represents the modeled fault. The scale is the same for all panels.

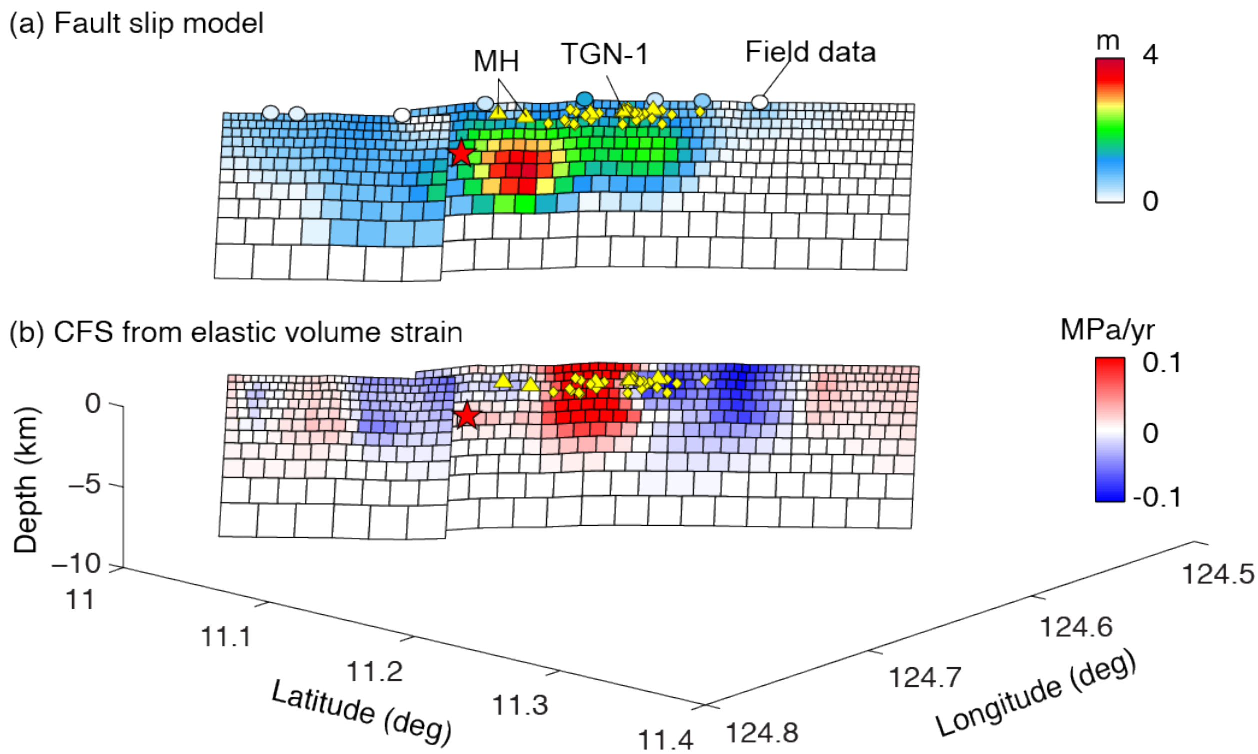

Fig. 3. Fault slip distribution model and Coulomb stress changes on the Leyte rupture zone. (a) coseismic fault slip model, Color-coded circles indicate the field observation results. (b) Stress changes due to elastic volume strain. Red star represents the hypocenter of the mainshock. Yellow triangles indicate the surface locations of the power plants, which are surrounded by numerous wells (diamonds).

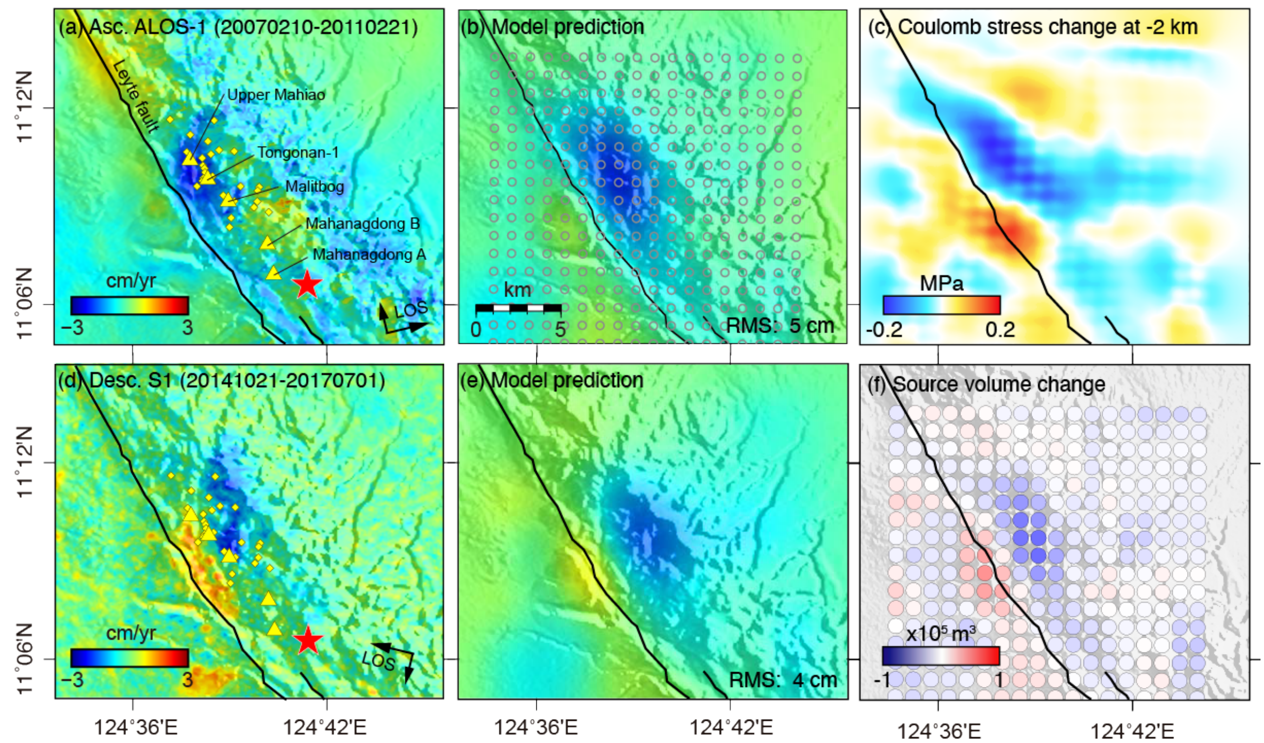

Fig. 4. Deformation and Coulomb stress changes near the 2017 Leyte rupture zone due to elastic strain from the net fluid extraction at the Tongonan geothermal field. Surface LOS displacement in (a) ascending-orbit ALOS-1 (2006-2011) and (d) descending-orbit Sentinel-1 (2014-2017) InSAR data. Negative values represent ground moving away from the satellite. Yellow triangles represent the locations of major power plants and yellow diamonds the wells. Black line represents the surface trace of the Leyte fault. (b and e) Predicted LOS surface displacements from the best-fitting Mogi source model. Gray circles represent source locations. (c) Coulomb stress changes at the hypocentral depth of 2 km due to the net fluid extraction assuming geometry of the mainshock. (f) Estimated source volume changes based on the best-fitting distributed Mogi source model. The integrated volume change is 1.7×10^6 m^3/yr.